Rotationally inelastic scattering of methyl radicals with Ar and N2

Ondřej Tkáč, Qianli Ma, Martin Stei, Andrew J. Orr-Ewing, and Paul J. Dagdigian

Citation: The Journal of Chemical Physics **142**, 014306 (2015); doi: 10.1063/1.4904901
View online: http://dx.doi.org/10.1063/1.4904901
View Table of Contents: http://scitation.aip.org/content/aip/journal/jcp/142/1?ver=pdfcov
Published by the AIP Publishing

Rotationally inelastic scattering of methyl radicals with Ar and N_2

Ondřej Tkáč,[1,a)] Qianli Ma (马千里),[2,b)] Martin Stei,[3] Andrew J. Orr-Ewing,[1,c)] and Paul J. Dagdigian[2,d)]
[1]*School of Chemistry, University of Bristol, Cantock's Close, Bristol BS8 1TS, United Kingdom*
[2]*Department of Chemistry, The Johns Hopkins University, Baltimore, Maryland 21218-2685, USA*
[3] *Institut für Ionenphysik und Angewandte Physik, Universität Innsbruck, Technikerstraße 25, 6020 Innsbruck, Austria*

(Received 8 November 2014; accepted 10 December 2014; published online 6 January 2015)

The rotationally inelastic scattering of methyl radical with Ar and N_2 is examined at collision energies of 330 ± 25 cm^{-1} and 425 ± 50 cm^{-1}, respectively. Differential cross sections (DCSs) were measured for different final n' rotational levels (up to $n' = 5$) of the methyl radicals, averaged over k' sub-levels, using a crossed molecular beam machine with velocity map imaging. For Ar as a collision partner, we present a newly constructed *ab initio* potential energy surface and quantum mechanical scattering calculations of state-resolved DCSs. These computed DCSs agree well with the measurements. The DCSs for both Ar and N_2 collision partners are strongly forward peaked for all spectroscopic lines measured. For scattering angles below 60°, the theoretical CD_3–Ar DCSs show diffraction oscillations that become less pronounced as n' increases, but these oscillations are not resolved experimentally. Comparisons are drawn with our recently reported DCSs for scattering of methyl radicals with He atoms. © *2015 AIP Publishing LLC.* [http://dx.doi.org/10.1063/1.4904901]

I. INTRODUCTION

Comparisons between experimental and computed differential cross sections (DCSs) for inelastic collisions critically test *ab initio* calculations of the potential energy surfaces (PESs) governing the intermolecular interactions. We recently reported studies of inelastic scattering of methyl radicals with He,[1] H_2, and D_2,[2] in which we contrasted the outcomes of crossed molecular beam scattering experiments with close coupling quantum mechanical (QM) scattering calculations. These studies explored the scattering-angle and quantum-state resolved scattering dynamics for a polyatomic radical for the first time. The experiments used resonance enhanced multiphoton ionization (REMPI) and velocity map imaging (VMI)[3,4] methods to capture angular scattering distributions for single final n' levels of the radical (with n the quantum number for rotational angular momentum of the molecular framework). However, the REMPI scheme limited the measurements to averaging over some or all of the final k' sub-levels corresponding to the projection of the rotational angular momentum on the threefold symmetry axis of the radical. Appropriate averaging of computed n, $k \rightarrow n'$, and k' state-to-state DCSs over the initial distribution of methyl radical levels populated in the molecular beam and final levels probed by REMPI and VMI allowed direct comparison of theory with experiment.

The excellent agreement validated the quality of the *ab initio* PESs for methyl–He and methyl–H_2 computed by Tkáč *et al.*,[2] and Dagdigian and Alexander.[5] Furthermore, we were able to draw robust conclusions about the scattering dynamics and propensities for different n and k changing collisions, and to trace these effects to properties of the PES, such as the polar and azimuthal anisotropies about the C_3 symmetry axis. Scattering of planar CD_3 with He was contrasted with the state-resolved dynamics of collisions of He with pyramidal ND_3.[6] This body of work extended the scope of inelastic scattering of labile free radicals, which had previously concentrated on collisions of diatomic radicals with atomic species.[7–25] A recent article by Dagdigian reviewed collisional energy transfer calculations for small hydrocarbon intermediates[26] and highlighted computational studies of integral cross sections for collisions of methylene (CH_2)[27,28] and methyl radicals.[5,28,29] The methyl radical is also the first polyatomic free radical to be slowed in a Zeeman decelerator using a pulsed magnetic field,[30] opening up new possibilities to study inelastic and reactive scattering at very low collision energies.

The collisions between methyl radicals and He or H_2 are largely controlled by repulsive interactions at the collision energies studied. In the current work, we replace these light collision partners with Ar and N_2 to explore the effects on the scattering of greater mass as well as the influence of attractive interactions in the intermolecular PES. The comparisons between Ar and N_2 examine the consequences of adding a rotational degree of freedom to the collision partner. The experimental measurements used the same methyl radical REMPI and VMI techniques as in our previous studies, but the theoretical component required computation of a new PES for CH_3–Ar prior to conducting QM scattering calculations.

Previous studies of inelastic scattering with Ar concentrated mostly on NO,[8–10,31–39] OH,[18,21,22,24] and HCl,[40] although scattering of a polyatomic molecule with Ar has been explored in the case of NH_3.[41,42] Molecular nitrogen was previously used

[a)]Present address: Laboratorium für Physikalische Chemie, ETH Zürich, CH-8093 Zürich, Switzerland.
[b)]Present address: Institut für Theoretische Chemie, Universität Stuttgart, Pfaffenwaldring 55, D-70569 Stuttgart, Germany.
[c)]Electronic mail: a.orr-ewing@bristol.ac.uk
[d)]Electronic mail: pjdagdigian@jhu.edu

as a collider in studies of the inelastic scattering of HCl.[43] Here, we present angular scattering distributions for CD_3–Ar at a collision energy of 330 ± 25 cm^{-1} and for CD_3–N_2 at 425 ± 50 cm^{-1}, measured by REMPI and VMI for final rotational levels of the methyl radical up to $n' = 5$. We adopt the same procedure as we used for CD_3 scattering with He, H_2, and, D_2 to compare the CD_3–Ar measurements with QM scattering calculations, and the good agreement confirms the quality of the newly developed PES.

II. METHOD

A. Experimental apparatus

Measurement of DCSs for inelastic scattering of methyl radicals with Ar and N_2 used a compact crossed molecular beam apparatus with VMI that has been described in detail previously.[1] In brief, supersonic expansion of gas mixtures through a pair of pulsed valves (General Valve Series 9) and collimation by skimmers produced the two molecular beams. Methyl radicals were generated in the primary beam by 266-nm photolysis of CH_3I or CD_3I entrained as a 3% mixture in Ar at a stagnation pressure of 4 bar. This photolysis occurred directly after the nozzle orifice to allow collisional cooling of the rotational and vibrational degrees of freedom of the radicals. Expansion of pure Ar or N_2 at 4 bar stagnation pressure produced the secondary beam of scattering partners. Experiments used a repeating mode of 50 shots with and 50 shots without the secondary beam, and the desired scattering signal was obtained by subtraction of a background image (obtained without Ar/N_2) from the total signal image.

The two molecular beams intersected at 90° within a high vacuum chamber, with the crossing region located in the extraction region of a 20-electrode stack of ion optics designed for dc slice-imaging.[44] Inelastically, scattered methyl radicals were ionized by a probe laser focused by a 30 cm lens to the intersection of the molecular beams. The static electric field from the ion optics accelerated the ions towards a position-sensitive detector (Photek) which consisted of a pair of microchannel plates (MCPs), a phosphor screen (P46 phosphor), and a CCD camera. A 20-ns voltage pulse applied to the rear MCP time-gated the detection of ions for mass resolution and velocity sliced imaging.

(2 + 1) REMPI detection of methyl radicals used UV radiation in the wavelength range 285-288 nm. Frequency doubling the output of a tuneable pulsed dye laser provided the wavelength-selected UV, and the energy and linewidth of this probe laser light were 4.5 mJ/pulse and 0.32 cm^{-1}, respectively. The resultant ions were accelerated towards the detector by a homogeneous electric field, which stretched the ion packet according to the initial velocity component of the neutral radicals perpendicular to the collision plane defined by the two molecular beams. Only a thin central slice of the ion packet was observed by the detector because of the short voltage pulse applied to the rear MCP. This slice corresponded to methyl radicals scattered within or close to the collision plane. The three dimensional velocity distribution of the inelastically scattered methyl radicals was retrieved directly from this slice image without the need for image reconstruction. The detection efficiency of the scattered products depended on their laboratory frame velocity, but this bias was corrected by a density-to-flux transformation using the method of Monte Carlo simulation of the experiment as described previously.[1,45]

B. Methyl radical initial state distribution and REMPI detection

The methyl radical is an oblate symmetric top, with rotations described by quantum numbers for total rotational angular momentum n and its body-frame projection k. As discussed in detail previously,[1] the CH_3 and CD_3 radicals exist in two and three nuclear spin modifications, respectively, and these nuclear-spin types do not interconvert during molecular collisions. The energies of low-lying rotational levels of CH_3 and CD_3 were plotted in Fig. 3 of Ref. 1. Fine-structure and hyperfine splittings are very small for the methyl radical[46] and are ignored in our theoretical treatment.

(2 + 1) REMPI detection of inelastically scattered CD_3 or CH_3 radicals used the well-established scheme of excitation via the 0_0^0 band of the $4p\ ^2A_2'' \leftarrow \tilde{X}\ ^2A_2''$ transition.[47,48] Determination of rotational level populations in the incident radical beam required comparison of experimental REMPI spectra with spectra simulated using the PGOPHER program.[49] We previously showed that the distribution of methyl radicals in the beam corresponds to a rotational temperature of ~15 K,[1] and relative populations of the rotational levels were presented in Table 1 of Ref. 1. The rovibrational levels of the excited $4p\ ^2A_2''$ electronic state are predissociated, resulting in broader linewidths and poorer detection efficiencies for the CH_3 isotopologue than for CD_3. Therefore, the work presented here concentrates on the inelastic scattering of CD_3; measured images and corresponding DCSs for the CH_3–Ar system can be found in the supplementary material (Figs. S1 and S2).[50]

The REMPI spectral lines for methyl are resolved in the n rotational quantum number, but not in the k projection quantum number, and the k projection levels of a given n contribute differently to different Δn spectroscopic branches. As in our previous work,[1,2,6] we employ the short-hand notation n_k to label rotational levels. We denote the unresolved n_{k_1},n_{k_2},… levels associated with a particular spectroscopic transition by $n_{k_1k_2}$… and recognize that these levels all contribute to the measured DCSs. The relative contributions of the different k levels were determined by PGOPHER calculation of 2-photon line strength factors.

C. CH_3–Ar potential energy surface

Similar to our previous treatment of the CH_3–He PES,[5] we describe the geometry of the CH_3–Ar complex with three coordinates, namely, the distance R of the atom from the center of mass of the molecule and the orientation, given by the angles (θ, ϕ). The body-frames z and x are chosen to lie along the C_3 axis and a C–H bond. This coordinate system is illustrated in Fig. 1 of Ref. 5. The potential is expanded as[5]

$$V(R,\theta,\phi) = \sum_{\lambda,\mu\geq 0} V_{\lambda\mu}(R)\left(1+\delta_{\mu 0}\right)^{-1} \times \left[Y_{\lambda\mu}(R) + (-1)^{\mu} Y_{\lambda,-\mu}(R)\right]. \quad (1)$$

The three-fold symmetry of CH_3 requires that μ be a multiple of 3, and the planar geometry of CH_3 requires that $\lambda + \mu$ be even.[5]

We performed explicitly correlated coupled-cluster calculations with inclusion of single, double, and (perturbatively) triple excitations [RCCSD(T)-F12a][51–53] for the CH_3–Ar PES. We employed the augmented correlation-consistent basis set aug-cc-pVTZ (aVTZ).[54,55] A counterpoise correction was applied for basis-set superposition error.[56,57] All calculations were carried out with the MOLPRO 2012.1 suite of programs.[58] In our previous investigations of the CH_3–He PES,[5] we employed conventional RCCSD(T) calculation using the aVQZ basis set with the addition of mid-bond functions[59,60] [RCCSD(T)/aVQZ+ BF]. To check the accuracy of the RCCSD(T)-F12a calculations, we performed additional calculations on 10 random orientations each at 7 atom-molecule separations. We found that the RCCSD(T)-F12a/aVTZ method gives interaction energies closer to the CBS limit [extrapolated from conventional RCCSD(T) calculations with the aVDZ, aVTZ, and aVQZ basis sets] at short to moderate R compared with the RCCSD(T)/aVQZ+ BF calculation. At larger R, the two methods give comparable interaction energies (differing by less than 0.1 cm^{-1} at $R = 15$ bohr). In addition, the former method is less computationally demanding.

The CH_3–Ar interaction energies were determined on a three-dimensional grid. The R grid includes 33 values of R (3.5–9 bohr, in steps of 0.25 bohr, 9.5, 10, 11, 12, 13, 14, 15, 16, 18, and 20 bohr). The θ grid contains 11 values from 0° to 90° defined by $\cos\theta = 0$ to 1, in steps of 0.1. The ϕ grid contains 7 values ranging from 0° to 60°, in steps of 10°. The total number of geometries for which the interaction potential was computed was 2541. For all the computations, the C–H bond length was fixed at $r_0 = 2.037$ bohr, which is the equilibrium bond length from RCCSD(T)/aug-cc-pVQZ calculations.[5]

In fitting the PES to Eq. (1), we included all symmetry allowed terms with $\lambda \leq 12$. The *ab initio* points were fitted with this 19-term angular basis using the least squares method. The quality of the fit was good. For all $R > 4.5$ bohr, the RMS error of the fit was less than 1% of the absolute value of the *ab initio* interaction energies averaged over the 77 orientations. At long range, the four larger expansion coefficients V_{00}, V_{33}, V_{20}, and V_{40} were extrapolated to AR^{-n}, with A and n determined from the fitted coefficients at $R = 18$ and 20 bohr. The values of n obtained for the four terms were 6.36, 6.29, 7.92, and 7.35, respectively. The expansion coefficient for the isotropic term is much larger (by a factor of >20 at $R = 20$ bohr) than the other coefficients at large R. An $R^{-6.36}$ dependence is a reasonable approximation for the isotropic term of the dispersion interaction $[c_6R^{-6} + c_8R^{-8} + \cdots]$,[61] confirming that the RCCSD(T)-F12a interaction energies have a reasonable long-range behavior. The fitted coefficients were switched to the long-range forms with a switching function centered at $R = 18$ bohr to ensure their smoothness over R.

Figure 1 displays a contour plot of the dependence of the potential energy upon the orientation of the argon atom for an atom-molecule separation $R = 6.75$ bohr. Like the CH_3–He PES (see Fig. 3 of Ref. 5), the CH_3–Ar PES displays a three-fold symmetry in ϕ, with maximum repulsion at orientations

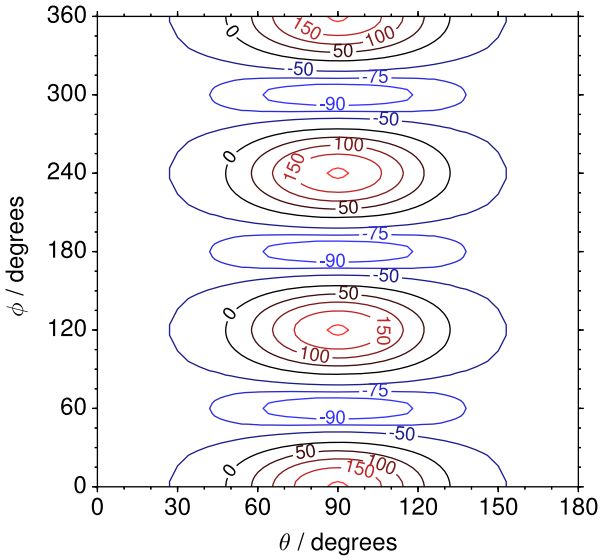

FIG. 1. Dependence of the potential energy (in cm^{-1}) on the orientation (θ, ϕ) of the argon atom with respect to the methyl radical for an atom-molecule separation $R = 6.75$ bohr.

for which the atom is near one of the H atoms. The potential is most attractive when the Ar atom is in the plane of the radical and bisecting a H–C–H angle. The global minimum of the CH_3–Ar PES is at $R = 7.13$ bohr, $\theta = 90°$, $\phi = 60°$, with a dissociation energy $D_e = 120.1$ cm^{-1}. The CH_3–He PES has a global minimum at a smaller value of R (6.52 bohr), with a much smaller D_e (27.0 cm^{-1}).[5] Since the center of mass of the methyl radical is at the carbon atom, the same PES can be used to describe the interaction of CD_3 with Ar.

Figure 2 presents a plot of the larger expansion coefficients as a function of the atom-molecule separation R. For moderate to large R, the isotropic V_{00} coefficient dominates, and the V_{33} and V_{20} coefficients are the largest anisotropic coefficients, as is the case for the CH_3–He PES.[5] In fact, the anisotropy of the two PESs is quite similar. The major differences lie in the larger magnitude of the expansion coefficients (hence stronger interactions) and the larger atom-molecule separation at which the minimum in the V_{00} coefficient occurs for the CH_3–Ar PES.

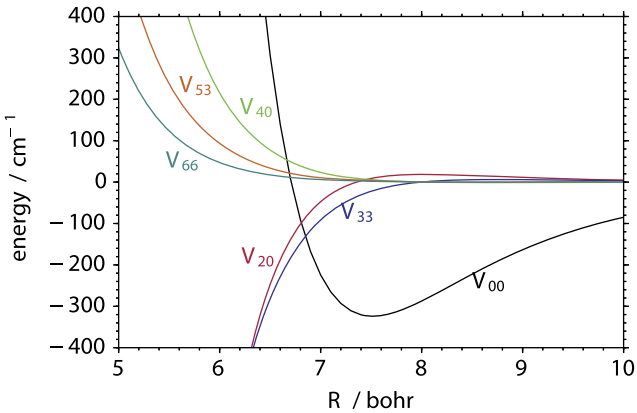

FIG. 2. Dependence of the larger expansion coefficients $V_{\lambda\mu}(R)$ [defined in Eq. (1)] upon the CH_3–Ar separation R.

D. Quantum scattering calculations

Calculations for collisions of the methyl radical with Ar atoms followed closely the procedures described previously for CH_3/CD_3–He scattering.[1,5] A brief description is provided here. We used the HIBRIDON suite of programs[62] to carry out time-independent quantum close-coupling spin-free calculations of state-resolved integral and differential cross sections. Rotational levels whose energies were less than 1000 cm^{-1} were included in the channel basis, and the scattering calculations included total angular momenta $J \leq 130\ \hbar$. The convergence of the cross sections was carefully checked. Separate calculations were carried out for the three nuclear spin modifications of CD_3.

Since the CD_3 incident beam included several rotational levels, DCSs for formation of a specific final rotational level $n'_{k'}$ were determined by weighting the computed state-to-state DCSs at the experimental collision energy by the experimentally determined incident beam rotational populations presented in Table 1 of Ref. 1. Computed state-to-state differential cross sections for the 1_1 initial level are presented in the supplementary material (Fig. S3).[50] As noted in Sec. II B, the k projection quantum number is not resolved in the REMPI spectra. Hence, theoretical DCSs for comparison with the experimental measurements were prepared by weighting the DCSs for the beam initial state distribution according to the 2-photon line strength factors for the given detection line.

It is interesting to compare the integral cross sections (ICSs) for CD_3–Ar and CD_3–He collisions. We present in Fig. 3 computed ICSs for transitions out of the lowest levels of the three CD_3 nuclear spin modifications, namely, 0_0 (A_2 nuclear spin symmetry), 1_0 (A_1 nuclear spin symmetry), and 1_1 (E nuclear spin symmetry), in collisions with Ar at a collision energy of 440 cm^{-1}. The final state propensities are almost identical to those for CD_3–He at the same collision energy (see Fig. 5 of Ref. 6). For both systems, the largest cross section for both the 0_0 and 1_0 initial levels is found for the transition to the 3_3 final level, while the 2_2 and 4_4 final levels have the largest cross sections for transitions from the 1_1 initial level. All these transitions are directly coupled by the V_{33} coefficient. The larger CD_3–Ar ICSs in Fig. 3 are approximately two times larger than the corresponding CD_3–He ICSs, consistent with the stronger interaction between CD_3 and Ar. The V_{20} and other $\mu = 0$ terms directly couple $\Delta k = 0$ transitions. The relative magnitude of the V_{20} term is somewhat larger for CD_3–Ar than for CD_3–He (compare the expansion coefficients of the former in Fig. 2 with those for CD_3–He in Fig. 4 of Ref. 5). However, we do not observe significant differences in the relative cross sections for $\Delta k = 0$ transitions.

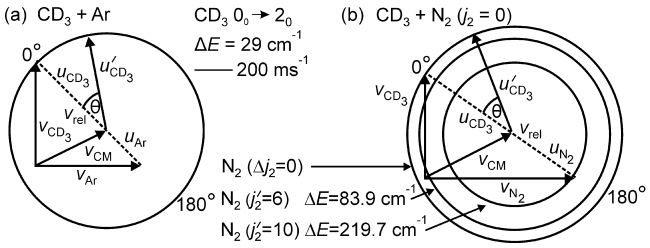

FIG. 4. Newton diagrams for inelastic scattering of CD_3 with (a) Ar and (b) N_2. The Newton spheres are drawn for inelastic scattering of CD_3 from the initial state $n_k = 0_0$ to the final state $n'_{k'} = 2_0$, which corresponds to an energy transfer of $\Delta E = 29.0\ cm^{-1}$. Three Newton spheres are drawn for N_2 final rotational angular momentum quantum numbers $j'_2 = 0$, 6, and 10 assuming that the initial state has $j_2 = 0$. The transfer of energy for transitions into these levels is indicated.

III. RESULTS

Figure 4 shows Newton diagrams for inelastic scattering of CD_3 with Ar and N_2 for the $0_0 \rightarrow 2_0$ transition. The Newton spheres are drawn for N_2 final rotational angular momenta $j'_2 = 0$, 6, and 10 assuming an initial rotational angular momentum quantum number $j_2 = 0$. This figure demonstrates that the Newton spheres for different final rotational states of N_2 would not be distinguishable in the measured images. The Newton spheres for $j'_2 = 0$–6 are almost overlapping because of the small rotational energy spacing. It is reasonable to assume that N_2 molecules are populated in several rotational levels in the beam after the supersonic expansion of pure N_2, which will further reduce the product kinetic energy resolution of the images. N_2 rotational levels with $j'_2 \leq 14$ are accessible following CD_3 collision with $N_2(j_2 = 0)$ at our experimental collision energy, and this limit on j'_2 may increase for collisions with $N_2(j_2 > 0)$ present in the secondary molecular beam. The experiment does not provide any information about the initial and final rotational angular momenta of N_2, and it is a degree of freedom we cannot control beyond the effects of cooling in the expansion, but we expect the initial rotational temperature of the N_2 molecules to be around 30 K.[63]

The higher mass of an Ar atom and lower velocity of the Ar beam with respect to He, H_2, and D_2 colliders used in our prior studies results in a smaller mean collision energy

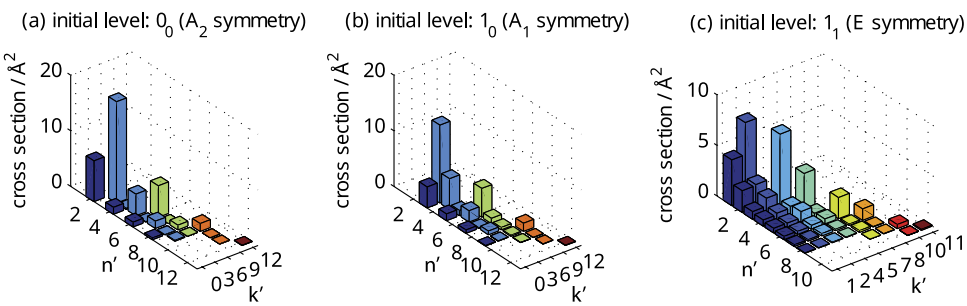

FIG. 3. Integral cross sections for transitions out of the lowest levels of CD_3 for each nuclear spin modification in collisions with Ar at a relative translational energy of 440 cm^{-1}. Since the cross sections for transitions to CD_3 high n' levels are small, the plots show cross sections for final levels with $n' \leq 12$.

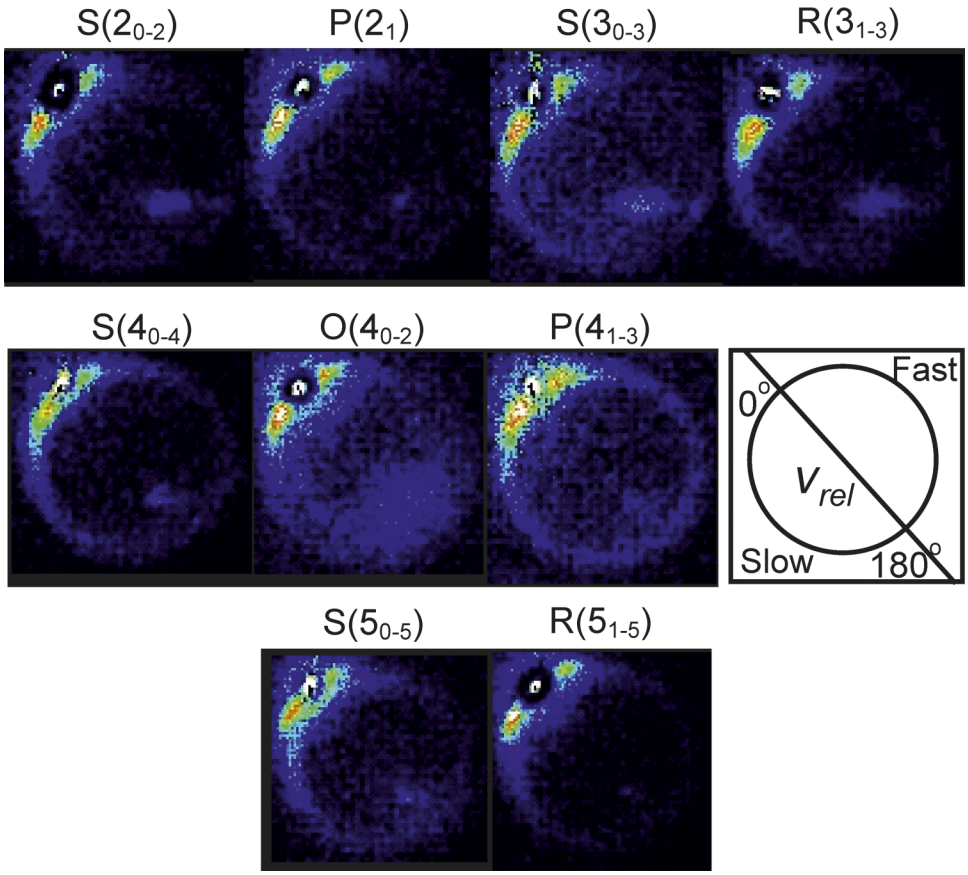

FIG. 5. Raw velocity map images for inelastic scattering of CD_3 radicals by Ar at a collision energy of 330 ± 25 cm^{-1}. The images are labelled by the symbol $Y\left(n'_{k'_1-k'_N}\right)$ for final rotational levels with n' = 2–5 for the CD_3 radical and unresolved final k' projection levels. Y denotes the spectroscopic branch. The orientation of the relative velocity vector v_{rel} is indicated in one panel.

$E_{coll} = 330 \pm 25$ cm^{-1}. Raw experimental images for inelastic scattering of CD_3 with Ar are shown in Fig. 5 for final rotational angular momentum levels up to $n' = 5$. Images for rotational levels with larger n' could not be measured because of the low collision energy. The intense spot in the images at angles close to 0° results from imperfect subtraction of signals from CD_3 populating the probed rotational level in the primary molecular beam. The spot around 180° present in some of the images is background that originates from the secondary (Ar) beam.

The unprocessed images directly demonstrate that the scattering is strongly forward peaked for all spectroscopic lines probed. This deduction is also clear from the DCSs extracted from the raw images by density-to-flux transformation. The derived DCSs are shown in Fig. 6, where they are compared with theoretical DCSs from the QM scattering calculations. For quantitative comparison with the theoretical calculations, the experimental DCSs were normalized by scaling the experimental value at a scattering angle of 90° to match the theoretical value at the same angle. This choice avoids normalization in the region of diffraction oscillations in the theoretical DCSs. The CD_3 molecules are almost exclusively scattered into the angular region $\theta \leq 60°$ in collisions with Ar for all measured final levels with final rotational angular momentum $n' \leq 5$.

Uncertainties in the experimental DCSs were determined by combining the standard deviation of values obtained from comparison of several separately measured images for a single final n' state with the uncertainty introduced by density-to-flux transformation of the raw data. This latter factor was quantified by comparing the magnitudes of the DCSs obtained from the two separate halves of the image at selected scattering angles. For perfect transformation, the extracted DCSs should be symmetric about the relative velocity vector.

Raw experimental images for inelastic scattering of CD_3 with N_2 into final levels with $n' = 2$–5 are shown in Fig. 7 for $E_{coll} = 425 \pm 50$ cm^{-1}. Inspection of these raw images reveals that they closely resemble the images measured for the CD_3–Ar system. Indeed, all of these images are strongly forward peaked and extend only as far as $\theta \sim 60°$, as can also be seen from the extracted DCSs plotted in Fig. 8. The DCSs are normalized to their maximum values for each spectroscopic line measured, and the error bars are determined in the same manner as for CD_3–Ar scattering.

The measured images for CD_3–N_2 are broader in the radial coordinate than images measured for inelastic scattering of CD_3 with Ar. This broadening can be attributed to transitions involving a change in the rotational level of N_2, which reduce the kinetic energy resolution of the images. Because of the small rotational constant for N_2 [$B(N_2) = 1.9982$ cm^{-1}][64] transitions involving a change in the N_2 rotational level would be expected to make a significant contribution to state-to-state DCSs.

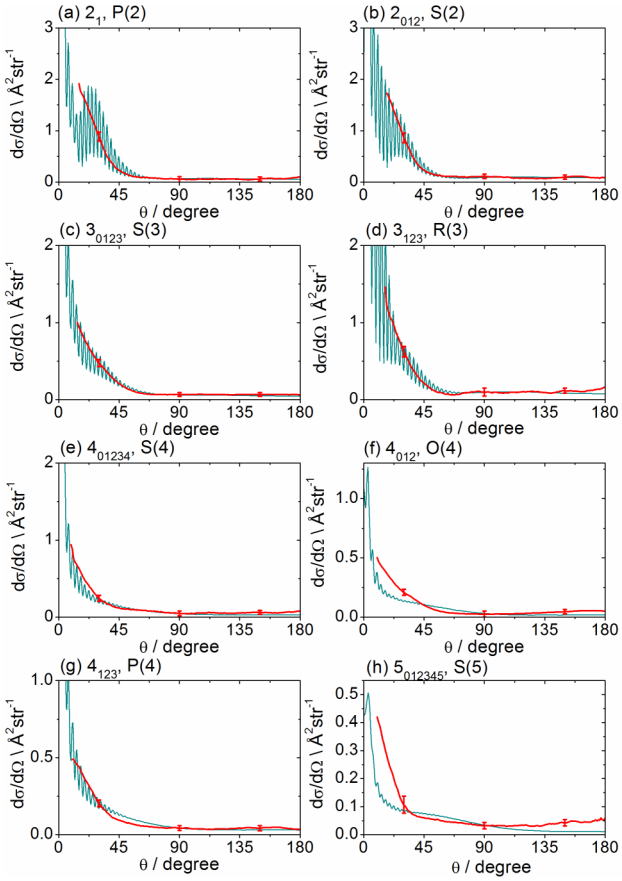

FIG. 6. Experimental (red) and theoretical (blue) DCSs for inelastic scattering of CD_3 radicals by Ar at a collision energy of 330 ± 25 cm^{-1} into final rotational levels n' = 2–5. The REMPI line employed for detection is indicated, along with the range of k' projection levels contributing to the scattering. The method of normalization of the experimental DCSs is described in the main text.

Scattering calculations were not performed for CD_3–N_2 since these calculations are extremely computationally demanding. Comparing with our earlier CD_3–H_2 calculations,[2] the smaller rotational constant of the heavier N_2 results in a significantly larger number of rotational levels and hence channels in close-coupling calculations. In addition, a CH_3–N_2 PES is not available at present.

IV. DISCUSSION

The DCSs computed for inelastic scattering of CD_3 into $n' = 2$–5 by collisions with Ar agree well with those obtained from the experimental measurements. In both cases, the scattering peaks strongly in the forward direction, and there is very little flux for scattering angles greater than 60°. This weak sideways and backward scattering is slightly enhanced for larger Δn collisions, reflecting a contribution from low impact parameters (or low angular momentum partial waves). The agreement between experimentally and theoretically derived DCSs confirms the high quality of the new CD_3–Ar PES at energies relevant to the current study.

There are subtle differences in the shapes of the DCSs obtained for CD_3 detection in a single n' level via different spectroscopic transitions. For example, the DCSs for $n' = 4$,

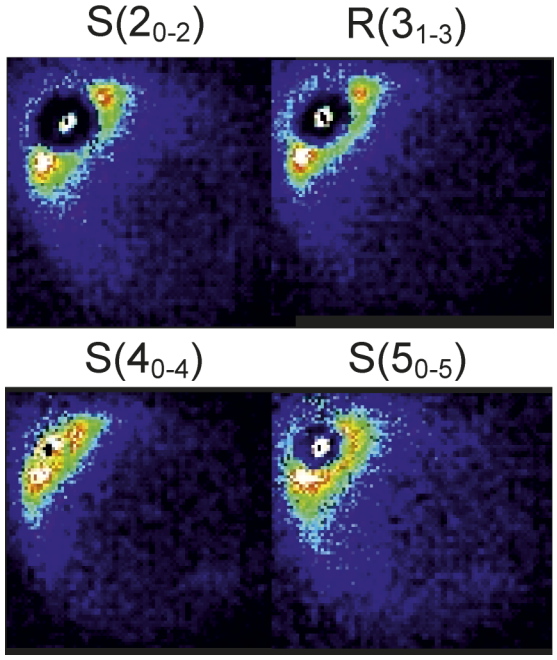

FIG. 7. Raw velocity map images for inelastic scattering of CD_3 radicals by N_2 at a collision energy of 425 ± 50 cm^{-1}. The notation used to label the images is defined in the caption to Fig. 5. Images are shown for final CD_3 rotational levels with n' = 2–5, with unresolved final k' projection levels.

obtained from measurements using the $S(4)$, $P(4)$, and $O(4)$ REMPI lines differ in the sharpness of the forward scattering into angles less than 45°. These small differences are a consequence of the distribution of k' sub-levels probed by REMPI, and the labels in Fig. 6 identify the particular subsets of k' contributing to each measured image. Changes in the scattering dynamics leading to population of different k' sub-levels for a given n' level can be explored by examination of the state-to-state DCSs obtained from the QM scattering calculations. We reported this type of analysis previously for CD_3–He scattering,[1] and Fig. 9 compares the computed DCSs

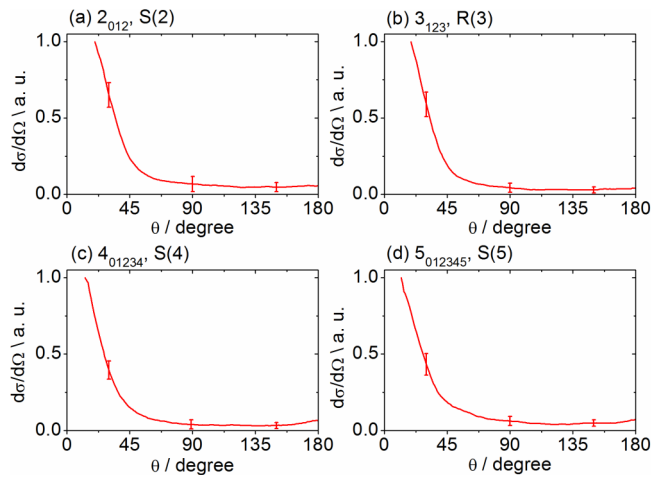

FIG. 8. Experimental DCSs for inelastic scattering of CD_3 radicals by N_2 at a collision energy of 425 ± 50 cm^{-1} into final rotational levels n' = 2–5. The REMPI line employed for detection is indicated, along with the range of k' projection levels contributing to the scattering. The experimental DCSs are normalized to their maximum values.

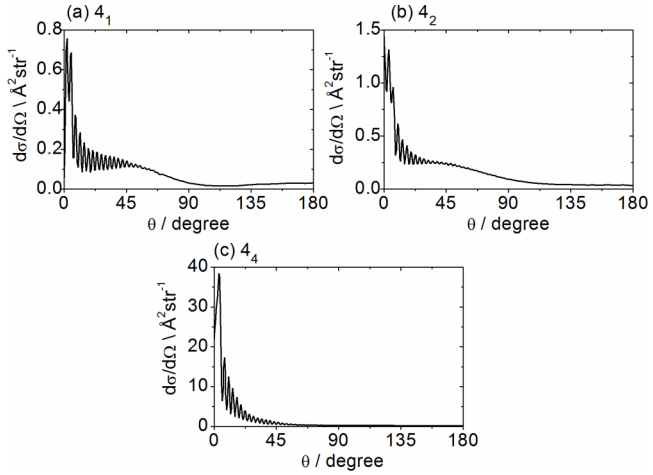

FIG. 9. Theoretical state-to-state CD_3–Ar inelastic DCSs out of the level $n_k = 1_1$ into levels with $n' = 4$ at a collision energy of 330 cm^{-1}.

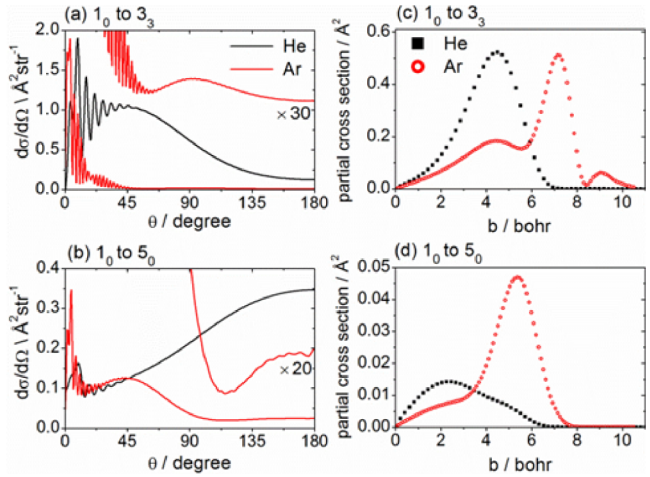

FIG. 10. (a) and (b) Computed state-to-state DCSs and (c) and (d) corresponding partial cross sections for inelastic scattering of CD_3 out of the 1_0 rotational level into 3_3 and 5_0 final levels in collisions with Ar and He at a collision energy of 440 cm^{-1}. The DCSs for CD_3–Ar were normalized to the same maximum value as the CD_3–He DCSs. The DCSs for CD_3–Ar are also shown magnified (using an angle-independent scaling) to highlight the small sideways and backward peaks for the 3_3 and 5_0 final levels, respectively.

for CD_3–Ar for scattering from the initial state $n_k = 1_1$ into the $n'_{k'} = 4_1$, 4_2, and 4_4 final levels. The DCSs for 4_1 and 4_2 final levels are sharply forward peaked, with broad shoulders at intermediate scattering angles, whereas the forward-peaked DCS for the 4_4 product gradually decreases to larger scattering angles without these shoulders. Analysis of the QM results shows that the scattering into the 4_4 final level occurs, on average, over larger impact parameters (partial cross sections), consistent with this observation if we assume that the orbital angular momentum is approximately the same as the total angular momentum of the CD_3–Ar complex.

Figure 10 shows computed DCSs for inelastic scattering of CD_3 out of the $n_k = 1_0$ initial level into 3_3 and 5_0 final levels with both Ar and He as collision partners at the same collision energy of 440 cm^{-1}. This collision energy corresponds to experimental conditions for our earlier study of CD_3–He scattering.[1] The computed CD_3–Ar DCSs at a collision energy of 440 cm^{-1} are not much changed from those obtained at 330 cm^{-1}, which is reasonable considering the steep repulsive wall of the CD_3– Ar PES. The spacings of the diffraction oscillations evident at small scattering angles are smaller for CD_3–Ar than for CD_3–He because of the larger mass of the collider Ar,[65] as well as a larger impact parameter (b). In a simplified hard-sphere model, the spacing of the diffraction oscillations $\Delta\theta$ in atom-molecular collisions is approximately given by $\pi/(kb)$, where k is the wavenumber.[66] The oscillation period would be smaller for a collision system with a larger reduced mass at the same collision energy.

The most striking difference between the CD_3–Ar and CD_3–He DCSs is the much greater propensity for forward scattering for the former. For the collision of CD_3 with Ar, scattering into angles $\theta < 60°$ dominates the measured and computed DCSs, whereas for collisions with the lighter He, the scattering extends across the full range of angles up to 180°, as demonstrated in Fig. 10(a), and peaks in the sideways or backward directions for $n' \geq 4$ [Fig. 10(b)]. According to our calculations, the lowest final rotational level produced by collisions of CD_3 (1_0) with Ar at a collision energy of 440 cm^{-1} for which backward scattering dominates is $n'_{k'} = 8_3$. For CD_3 (1_0)–He, it is $n'_{k'} = 5_0$. The maximum in the partial cross section (PCS) distribution for this CD_3–Ar transition is at an impact parameter of $b = 5.5$ bohr.

The origin of the differences in DCSs for CD_3–Ar and CD_3-He lies in the PESs that govern the scattering dynamics. To visualize better the differences between the CH_3–He and CH_3–Ar PESs, we plot in Fig. 11 the dependence of these potentials upon R and ϕ, averaged over θ, shown as contours in the plane containing the CH_3 molecule. In the plots, a C–H bond is aligned with the positive direction of the x axis. The green contour corresponds to 440 cm^{-1}, which is the collision energy of the CD_3–He experiment[1] and the calculations described above. We see in Fig. 11 that the CH_3–Ar PES is more attractive at larger atom-molecule separations and the gradient of the potential in the attractive regions of the PES is larger.

The more forward character of the CD_3–Ar DCSs in Fig. 10 is likely due to the more attractive nature of the PES for this system. While the collision energy is much greater than the well depth, glancing collisions at large impact parameters that sample the attractive part of the potential can induce changes in the rotational angular momentum and contribute to small-angle scattering. Collisions of CD_3 with He are instead dominated by repulsive interactions and have relatively broad DCSs.

We note also that the duration of the collision is greater for the heavier Ar collider, mainly because of the smaller relative velocity than for light He. The transfer of angular momentum is classically directly proportional to the duration of the collision and to the gradient of the potential.[67] This difference in angular momentum transfer is reflected in the larger magnitudes of the CD_3–Ar state-to-state cross sections and, to a lesser extent, in the degree of rotational excitation of the CD_3 products [compare the CD_3–Ar state-to-state cross sections in Fig. 3 with the corresponding CD_3–He cross sections in Fig. 5 of Ref. 6].

Figures 10(c) and 10(d) compare PCSs for the 1_0–3_3 and 5_0 transitions for both collision partners. Similar to our

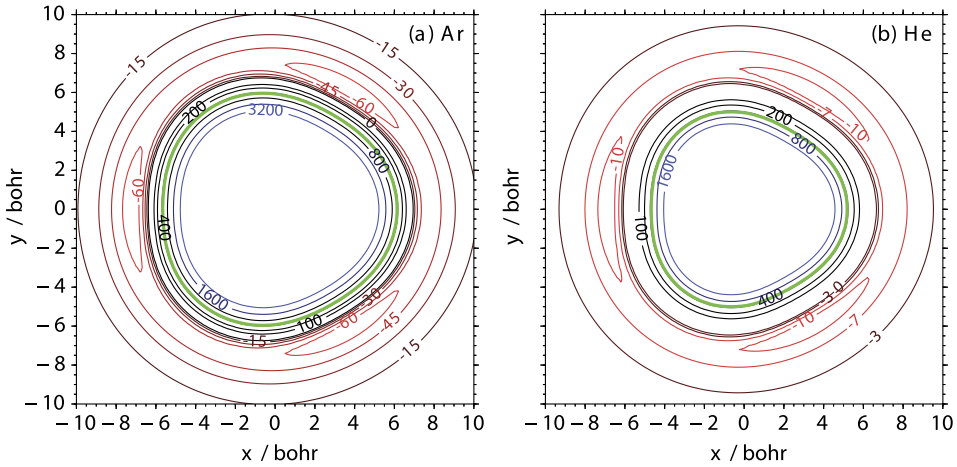

FIG. 11. Contour plots showing the dependence of the (a) CH_3–Ar and (b) CH_3–He PES upon R and ϕ, averaging over θ, projected onto the plane of the molecule. The green contour represents 440 cm^{-1}, which is the collision energy used in this work to compare the CH_3–Ar and CH_3–He DCSs.

previous treatment, we assume the orbital angular momentum of the CD_3–Ar complex is approximately its total angular momentum, which allows us to show the contributions to the ICS from various ranges of classical impact parameters. The inelastic scattering occurs at much larger orbital angular momentum, and hence impact parameter, for Ar as a collision partner than for He. We see in Fig. 10(d) that the maxima in the PCSs for the 1_0–5_0 transition occur for $b = 2.3$ and 5.5 bohr for He and Ar, respectively. This difference is mainly due to the greater radial extent of the CD_3–Ar PES [compare the contour plots of the CD_3–He and CD_3–Ar PESs in Fig. 11].

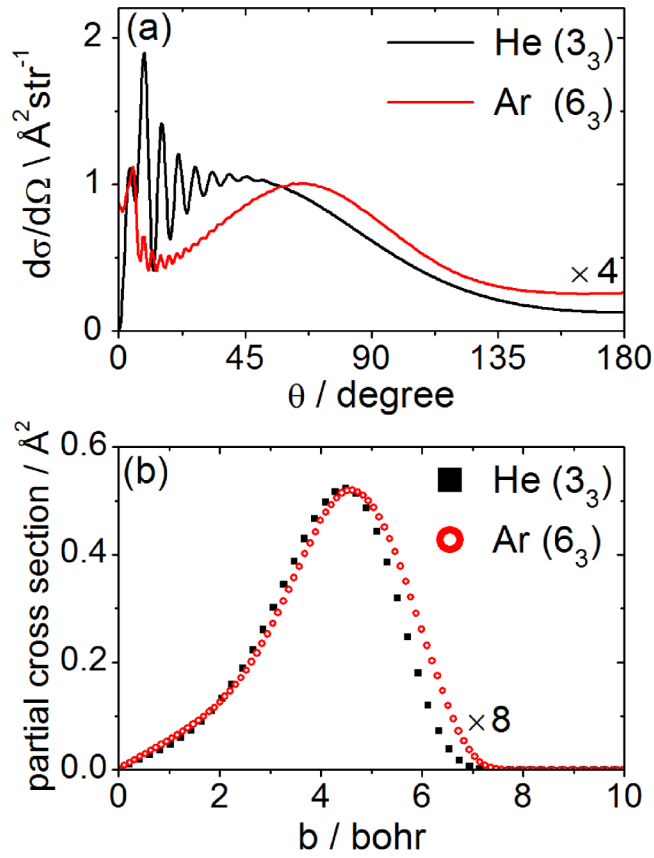

FIG. 12. (a) Computed state-to-state DCSs and (b) corresponding partial cross sections for inelastic scattering of CD_3 with He for the 1_0–3_3 transition and with Ar for the 1_0–6_3 transition at a collision energy of 440 cm^{-1}. The CD_3–Ar DCS was multiplied by factor of 4 and the partial cross section by a factor of 8 to assist the comparison.

To judge how well the angular scattering can be interpreted in terms of the classical impact parameter distribution, we compare two distinct $n_k \rightarrow n'_{k'}$ transitions for CD_3–Ar and CD_3–He that happen to occur over the same range of impact parameters. Figure 12 shows computed state-to-state DCSs and the corresponding PCSs for one such example. In this case, the $1_0 \rightarrow 3_3$ transition in CD_3–He and $1_0 \rightarrow 6_3$ transition for CD_3–Ar are compared. The two transitions both occur over a range of impact parameters that peaks at around 4.5 bohr, and the resulting DCSs are indeed very similar. Note that the CD_3–Ar DCS was multiplied by a factor of 4 and the partial cross section by a factor of 8 for the purposes of the comparison, and that both transitions involve $\Delta k = 3$.

The preceding comparison of inelastic scattering of methyl radical with heavy (Ar) and light (He) atomic colliders also holds for collisions with heavy (N_2) and light (D_2 or H_2) diatomic molecules. The broad DCSs measured for H_2 and D_2 collision partners contrast with the strongly forward peaking DCSs observed for collisions with N_2. The root cause of this greater propensity for forward scattering is again likely to be longer-range attractive interactions associated with the methyl–N_2 intermolecular potential. The larger polarizability of the N_2 collision partner[68] results in a greater intermolecular well depth and range of the attractive potential than for D_2 or H_2, and at the lower collision energies in the CD_3–N_2 system, the colliders sample more of the longer range regions of the PES. Therefore, the scattering will be influenced more heavily by attractive forces.

V. CONCLUSION

Experimentally determined differential cross sections for the rotationally inelastic scattering of CD_3 radicals by Ar compare very favorably with theoretical predictions obtained from close-coupling QM scattering calculations on a newly computed potential energy surface. This agreement confirms the quality of the new CD_3–Ar PES. The experimental measurements are resolved at the level of the final rotational angular momentum of the CD_3 radical (n') but are averaged over some or all of the final k' levels corresponding to projection of the

angular momentum on the symmetry axis of the radical. The QM scattering results can be examined at the full state-to-state level to explore trends in the scattering dynamics that depend on the magnitudes of the collision-induced changes Δn and Δk. The scattering calculations also reveal pronounced diffraction oscillations at scattering angles $\theta < 45°$ that are averaged out under our experimental conditions.

The flux of CD_3 scattered by Ar peaks strongly in the forward direction, with little or no amplitude for $\theta > 60°$ for the final levels $n' = 2$–5 probed. This behavior contrasts with the broad angular scattering observed previously in CD_3–He collisions, which are dominated by repulsive interactions. The greater propensity for forward scattering in the case of CD_3–Ar is a consequence of the greater importance of long-range attractive interactions that induce changes in the rotational angular momentum of the CD_3 for glancing (large impact parameter) collisions. In contrast to CD_3–He scattering, the DCSs for CD_3–Ar at our chosen collision energy show only a weak dependence on the final values of n' and k' quantum numbers.

Velocity map images for CD_3–N_2 scattering reveal DCSs that are qualitatively very similar to those for CD_3–Ar collisions. However, the images are broadened in the radial (speed) coordinate because of unresolved changes to the rotational energy of the N_2 collider. Comparison with prior CD_3–D_2 measurements shows a similar trend to substitution of Ar for He in collisions with CD_3: the heavier and more polarizable diatomic molecule promotes stronger forward scattering of the CD_3 because of more attractive long-range interactions.

ACKNOWLEDGMENTS

The Bristol group acknowledges EPSRC Programme Grant No. EP/G00224X for financial support and the EU Marie Curie Initial Training Network *ICONIC* for Early Career Researcher positions for O.T. and M.S. We are grateful to Stuart J. Greaves for valuable contributions to the design of the crossed beam and VMI apparatus. The theoretical portion of this work was supported by the Chemical, Geosciences, and Biosciences Division, Office of Basic Energy Sciences, Office of Science, U.S. Department of Energy under Grant No. DESC0002323. The authors gratefully acknowledge the advice and encouragement of Millard H. Alexander.

[1]O. Tkáč, A. K. Sage, S. J. Greaves, A. J. Orr-Ewing, P. J. Dagdigian, Q. Ma, and M. H. Alexander, Chem. Sci. **4**(11), 4199–4211 (2013).
[2]O. Tkáč, Q. Ma, C. A. Rusher, S. J. Greaves, A. J. Orr-Ewing, and P. J. Dagdigian, J. Chem. Phys. **140**, 204318 (2014).
[3]D. W. Chandler and P. L. Houston, J. Chem. Phys. **87**(2), 1445–1447 (1987).
[4]A. Eppink and D. H. Parker, Rev. Sci. Instrum. **68**(9), 3477–3484 (1997).
[5]P. J. Dagdigian and M. H. Alexander, J. Chem. Phys. **135**(6), 064306 (2011).
[6]O. Tkáč, A. J. Orr-Ewing, P. J. Dagdigian, M. H. Alexander, J. Onvlee, and A. van der Avoird, J. Chem. Phys. **140**(13), 134308 (2014).
[7]F. J. Aoiz, J. E. Verdasco, M. Brouard, J. Kłos, S. Marinakis, and S. Stolte, J. Phys. Chem. A **113**(52), 14636–14649 (2009).
[8]M. Brouard, H. Chadwick, C. J. Eyles, B. Hornung, B. Nichols, F. J. Aoiz, P. G. Jambrina, and S. Stolte, J. Chem. Phys. **138**(10), 104310 (2013).
[9]M. Brouard, H. Chadwick, C. J. Eyles, B. Hornung, B. Nichols, F. J. Aoiz, P. G. Jambrina, S. Stolte, and M. P. de Miranda, J. Chem. Phys. **138**(10), 104309 (2013).
[10]C. J. Eyles, M. Brouard, C. H. Yang, J. Kłos, F. J. Aoiz, A. Gijsbertsen, A. E. Wiskerke, and S. Stolte, Nat. Chem. **3**(8), 597–602 (2011).
[11]J. J. Kay, J. D. Steill, J. Kłos, G. Paterson, M. L. Costen, K. E. Strecker, K. G. McKendrick, M. H. Alexander, and D. W. Chandler, Mol. Phys. **110**(15-16), 1693–1703 (2012).
[12]J. Kłos, F. J. Aoiz, J. E. Verdasco, M. Brouard, S. Marinakis, and S. Stolte, J. Chem. Phys. **127**(3), 031102 (2007).
[13]H. Kohguchi, T. Suzuki, and M. H. Alexander, Science **294**(5543), 832–834 (2001).
[14]A. Gijsbertsen, H. Linnartz, G. Rus, A. E. Wiskerke, S. Stolte, D. W. Chandler, and J. Kłos, J. Chem. Phys. **123**(22), 224305 (2005).
[15]M. S. Westley, K. T. Lorenz, D. W. Chandler, and P. L. Houston, J. Chem. Phys. **114**(6), 2669–2680 (2001).
[16]M. Kirste, L. Scharfenberg, J. Kłos, F. Lique, M. H. Alexander, G. Meijer, and S. Y. T. van de Meerakker, Phys. Rev. A **82**(4), 042717 (2010).
[17]S. Marinakis, G. Paterson, J. Kłos, M. L. Costen, and K. G. McKendrick, Phys. Chem. Chem. Phys. **9**(31), 4414–4424 (2007).
[18]G. Paterson, S. Marinakis, M. L. Costen, K. G. McKendrick, J. Kłos, and R. Tobola, J. Chem. Phys. **129**(7), 074304 (2008).
[19]Z. Pavlovic, T. V. Tscherbul, H. R. Sadeghpour, G. C. Groenenboom, and A. Dalgarno, J. Phys. Chem. A **113**(52), 14670–14680 (2009).
[20]K. Schreel and J. J. ter Meulen, J. Chem. Phys. **105**, 4522 (1996).
[21]M. Brouard, A. Bryant, Y. P. Chang, R. Cireasa, C. J. Eyles, A. M. Green, S. Marinakis, F. J. Aoiz, and J. Klos, J. Chem. Phys. **130**(4), 044306 (2009).
[22]M. Brouard, H. Chadwick, Y. P. Chang, C. J. Eyles, F. J. Aoiz, and J. Kłos, J. Chem. Phys. **135**(8), 084306 (2011).
[23]L. Scharfenberg, K. B. Gubbels, M. Kirste, G. C. Groenenboom, A. van der Avoird, G. Meijer, and S. Y. T. van de Meerakker, Eur. Phys. J. D **65**(1-2), 189–198 (2011).
[24]M. C. van beek, J. J. ter Meulen, and M. H. Alexander, J. Chem. Phys. **113**(2), 628–636 (2000).
[25]G. Sarma, S. Marinakis, J. J. ter Meulen, D. H. Parker, and K. G. McKendrick, Nat. Chem. **4**(12), 985–989 (2012).
[26]P. J. Dagdigian, Int. Rev. Phys. Chem. **32**, 229–265 (2013).
[27]L. Ma, M. H. Alexander, and P. J. Dagdigian, J. Chem. Phys. **134**(15), 154307 (2011).
[28]L. Ma, P. J. Dagdigian, and M. H. Alexander, J. Chem. Phys. **136**, 224306 (2012).
[29]Q. Ma, P. J. Dagdigian, and M. H. Alexander, J. Chem. Phys. **138**, 104317 (2013).
[30]T. Momose, Y. Liu, S. Zhou, P. Djuricanin, and D. Carty, Phys. Chem. Chem. Phys. **15**, 1772 (2013).
[31]P. Andresen, H. Joswig, H. Pauly, and R. Schinke, J. Chem. Phys. **77**(4), 2204–2205 (1982).
[32]J. I. Cline, K. T. Lorenz, E. A. Wade, J. W. Barr, and D. W. Chandler, J. Chem. Phys. **115**(14), 6277–6280 (2001).
[33]M. J. L. de Lange, M. Drabbels, P. T. Griffiths, J. Bulthuis, S. Stolte, and J. G. Snijders, Chem. Phys. Lett. **313**(3-4), 491–498 (1999).
[34]C. J. Eyles, M. Brouard, H. Chadwick, F. J. Aoiz, J. Kłos, A. Gijsbertsen, X. Zhang, and S. Stolte, Phys. Chem. Chem. Phys. **14**(16), 5420–5439 (2012).
[35]C. J. Eyles, M. Brouard, H. Chadwick, B. Hornung, B. Nichols, C. H. Yang, J. Kłos, F. J. Aoiz, A. Gijsbertsen, A. E. Wiskerke, and S. Stolte, Phys. Chem. Chem. Phys. **14**(16), 5403–5419 (2012).
[36]J. J. Kay, G. Paterson, M. L. Costen, K. E. Strecker, K. G. McKendrick, and D. W. Chandler, J. Chem. Phys. **134**(9), 091101 (2011).
[37]G. Paterson, A. Relf, M. L. Costen, K. G. McKendrick, M. H. Alexander, and P. J. Dagdigian, J. Chem. Phys. **135**(23), 234304 (2011).
[38]A. G. Suits, L. S. Bontuyan, P. L. Houston, and B. J. Whitaker, J. Chem. Phys. **96**(11), 8618–8620 (1992).
[39]J. J. van Leuken, J. Bulthuis, S. Stolte, and J. G. Snijders, Chem. Phys. Lett. **260**(5-6), 595–603 (1996).
[40]T. K. Lorenz, M. S. Westley, and D. W. Chandler, Phys. Chem. Chem. Phys. **2**(4), 481–494 (2000).
[41]H. Meyer, J. Chem. Phys. **101**(8), 6697–6707 (1994).
[42]J. Schleipen, J. J. ter Meulen, G. C. M. van der Sanden, P. E. S. Wormer, and A. van der Avoird, Chem. Phys. **163**(2), 161–172 (1992).
[43]E. A. Wade, K. T. Lorenz, J. L. Springfield, and D. W. Chandler, J. Phys. Chem. A **107**(25), 4976–4981 (2003).
[44]D. Townsend, M. P. Minitti, and A. G. Suits, Rev. Sci. Instrum. **74**(4), 2530–2539 (2003).
[45]C. J. Eyles, D. Phil. thesis, University of Oxford, 2010.
[46]S. Davis, D. T. Anderson, G. Duxbury, and D. J. Nesbitt, J. Chem. Phys. **107**, 5661–5675 (1997).
[47]I. Powis and J. F. Black, J. Phys. Chem. A **93**(6), 2461–2470 (1989).
[48]J. F. Black and I. Powis, J. Chem. Phys. **89**(7), 3986–3992 (1988).

[49]C. M. Western, *PGOPHER,* a program for simulating rotational structure University of Bristol, 2014, http://pgopher.chm.bris.ac.uk.
[50]See supplementary material at http://dx.doi.org/10.1063/1.4904901 for raw images for CH_3-Ar raw images derived differential cross sections as well as the theoretical state-to-state differential cross sections for CD_3-Ar collisions.
[51]T. B. Adler, G. Knizia, and H.-J. Werner, J. Chem. Phys. **127**, 221106 (2007).
[52]G. Knizia and H. J. Werner, J. Chem. Phys. **128**(15), 154103 (2008).
[53]G. Knizia, T. B. Adler, and H.-J. Werner, J. Chem. Phys. **130**, 054104 (2009).
[54]T. H. Dunning, Jr., J. Chem. Phys. **90**, 1007 (1989).
[55]D. E. Woon and T. H. Dunning, J. Chem. Phys. **98**(2), 1358–1371 (1993).
[56]S. F. Boys and F. Bernardi, Mol. Phys. **19**(4), 553 (1970).
[57]F. B. van Duijneveldt, J. G. C. M van Duijneveldt-van de Rijdt, and J. H. van Lenthe, Chem. Rev. **94**, 1873–1885 (1994).
[58]H.-J. Werner, P. J. Knowles, R. Lindh, F. R. Manby, M. Schütz *et al.*, MOLPRO, version 2012.1, a package of *ab initio* programs, 2012, see http://www.molpro.net.
[59]F. M. Tao and Y. K. Pan, J. Chem. Phys. **97**(7), 4989–4995 (1992).
[60]H. Koch, B. Fernandez, and O. Christiansen, J. Chem. Phys. **108**(7), 2784–2790 (1998).
[61]R. P. Leavitt, J. Chem. Phys. **72**(6), 3472–3482 (1980).
[62]M. H. Alexander, D. E. Manolopoulos, H.-J. Werner, B. Follmeg, P. J. Dagdigian, and Q. Ma, HIBRIDON is a package of programs for the time-independent quantum treatment of inelastic collisions and photodissociation. More information and/or a copy of the code can be obtained from the website http://www2.chem.umd.edu/groups/alexander/hibridon.
[63]H. Mori, H. Yamaguchi, K. Kataoka, N. Sugiyama, K. Ide, and T. Niimi, AIP Conf. Proc. **1084**(1), 551–556 (2008).
[64]R. R. Laher and F. R. Gilmore, J. Phys. Chem. Ref. Data **20**(4), 685–712 (1991).
[65]A. von Zastrow, J. Onvlee, S. N. Vogels, G. C. Groenenboom, A. van der Avoird, and S. Y. T. van de Meerakker, Nat. Chem. **6**(3), 216–221 (2014).
[66]U. Buck, F. Huisken, and J. Schleusener, J. Chem. Phys. **68**(12), 5654–5655 (1978).
[67]S. Bosanac, Phys. Rev. A **26**(2), 816–824 (1982).
[68]R. D. Levine, *Molecular Reaction Dynamics* (Cambridge University Press, Cambridge, 2005).